

Journal of
Applied Remote Sensing



RemoteSensing.SPIEDigitalLibrary.org



Hyperspectral image super-resolution: a hybrid color mapping approach

Jin Zhou
Chiman Kwan
Bence Budavari

SPIE.

Jin Zhou, Chiman Kwan, Bence Budavari, "Hyperspectral image super-resolution: a hybrid color mapping approach," *J. Appl. Remote Sens.* **10**(3), 035024 (2016), doi: 10.1117/1.JRS.10.035024.

Hyperspectral image super-resolution: a hybrid color mapping approach

Jin Zhou,^a Chiman Kwan,^{b,*} and Bence Budavari^b

^aGoogle Inc., 1600 Amphitheatre Parkway, Mountain View, California 94043, United States

^bSignal Processing, Inc., 9605 Medical Center Drive, Rockville, Maryland, United States

Abstract. NASA has been planning a hyperspectral infrared imager mission which will provide global coverage using a hyperspectral imager with 60-m resolution. In some practical applications, such as special crop monitoring or mineral mapping, 60-m resolution may still be too coarse. There have been many pansharpening algorithms for hyperspectral images by fusing high-resolution (HR) panchromatic or multispectral images with low-resolution (LR) hyperspectral images. We propose an approach to generating HR hyperspectral images by fusing high spatial resolution color images with low spatial resolution hyperspectral images. The idea is called hybrid color mapping (HCM) and involves a mapping between a high spatial resolution color image and a low spatial resolution hyperspectral image. Several variants of the color mapping idea, including global, local, and hybrid, are proposed and investigated. It was found that the local HCM yielded the best performance. Comparison of the local HCM with >10 state-of-the-art algorithms using five performance metrics has been carried out using actual images from the air force and NASA. Although our HCM method does not require a point spread function (PSF), our results are comparable to or better than those methods that do require PSF. More importantly, our performance is better than most if not all methods that do not require PSF. After applying our HCM algorithm, not only the visual performance of the hyperspectral image has been significantly improved, but the target classification performance has also been improved. Another advantage of our technique is that it is very efficient and can be easily parallelized. Hence, our algorithm is very suitable for real-time applications. © 2016 Society of Photo-Optical Instrumentation Engineers (SPIE) [DOI: [10.1117/1.JRS.10.035024](https://doi.org/10.1117/1.JRS.10.035024)]

Keywords: super-resolution; hyperspectral; hybrid color mapping; pansharpening.

Paper 16326 received May 2, 2016; accepted for publication Sep. 1, 2016; published online Sep. 23, 2016.

1 Introduction

Hyperspectral images have gained popularity in remote sensing,^{1–4} target detection,^{5–7} anomaly,^{8–13} and change detection^{14–17} in recent years. Recently, we investigated the idea of applying super-resolution (SR) techniques to improve the spatial resolution of hyperspectral images, which are then used for anomaly and change detection.¹⁴ One SR method we used was the classical normalized convolution method,¹⁸ which utilizes multiple low-resolution (LR) views to reconstruct a high spatial resolution image. Results showed that the SR did enhance the performance of change detection slightly. In practice, this multiview-based approach is numerically limited only to a small increase in resolution.^{19,20} Moreover, the improvement in classification is very low.¹⁴

To break the limitation of classical methods, “example-based super-resolution” was proposed.^{21,22} In this technique, correspondences between LR and high-resolution (HR) image patches are first learned from a database of LR and HR image pairs. Unlike classical SR,¹⁸ the reconstructed HR details are not guaranteed to be the same as the true details. In addition, this technique is usually slow due to the time-consuming learning process. Another difficulty for hyperspectral images is that it is hard to find training sources. We implemented

*Address all correspondence to: Chiman Kwan, E-mail: chiman.kwan@signalpro.net

this approach and observed very little enhancement in terms of classification accuracy after SR.¹⁴

In the remote sensing domain, a common and successful approach to achieving SR is pansharpening.^{23–37} Pansharpening is an image fusion technique, which uses a high spatial resolution single-band panchromatic (pan) image and low spatial resolution multispectral to produce high spatial resolution multispectral images. Recently, pansharpening has been extended to hyperspectral images.^{26–38} Compared to multiview based techniques¹⁸ and example-based SR techniques,^{21,22} pansharpening can produce much higher resolution images and is much more reliable and accurate. In this paper, we propose an approach that uses the high spatial resolution bands of color images to reconstruct high spatial resolution hyperspectral images. The motivation is practical: there are many satellite sensors or airborne sensors which take HR color images or HR multispectral images (LANDSAT). For instance, the resolution of Google Map's color image data (Geo-eye) is 0.5 m.³⁹ We may combine those data with hyperspectral infrared imager (HypIRI), a future NASA satellite hyperspectral imager with 60-m spatial resolution data, to generate HR hyperspectral images. Specifically, we propose a method called hybrid color mapping (HCM) which is efficient and parallelizable. We performed extensive studies and our results showed that our method can generate accurate HR reconstruction. Comparison with >10 hyperspectral pansharpening algorithms shows that our algorithm performance is among the top few methods using five performance metrics. We divided the other methods into three groups. Group 1 contains methods that require a point spread function (PSF) and a pan band or some multispectral bands. Group 2 methods do not require PSF, but require a pan band. Group 3 methods do not require PSF or a pan band. Our HCM method is comparable to or better (in some cases) than those methods in Group 1. However, it must be emphasized that our HCM does not require PSF. Compared to those Group 2 methods, our HCM method performed the best in four out of five performance metrics for the air force (AF) image and performed close to those top performers for the AVIRIS image. For those Group 3 methods, our HCM performed better in most performance metrics for both AF and AVIRIS images. In addition, we also performed a very thorough classification study using reconstructed SR data. Classification results also show that our method performs among the best methods.

This paper is organized as follows. Section 2 introduces our proposed color mapping idea and its variants. Section 3 includes extensive comparative studies to demonstrate the performance of our algorithms. Finally, we conclude our paper with some highlights and suggestions for future research.

2 Super-Resolution Hyperspectral Image Generation Algorithm

2.1 Color Mapping

The idea of color mapping is as the name suggests: mapping of a color pixel $c_{(i,j)}$ at location (i, j) with R, G, B bands to a hyperspectral pixel $X_{(i,j)}$ at the same location. This mapping is based on a transformation matrix T , i.e.,

$$X_{(i,j)} = Tc_{(i,j)}, \quad (1)$$

where $X_{(i,j)} \in R^N$ is a single hyperspectral pixel with N spectral bands, $T \in R^{N \times M}$, $c_{(i,j)} \in R^M$ is a color pixel with M spectral bands, and $N \gg M$. Figure 1 shows the system flow. Given an HR color image and an LR hyperspectral image, our goal is to generate an HR hyperspectral image. To get the transformation matrix, we simulate an LR color image by down-sampling the HR color image. We then use the LR color image and the LR hyperspectral image to train the T . Once T is obtained, it can then be used for generating the HR hyperspectral image pixel by pixel.

Let us denote H as the set of all hyperspectral pixels $X_{(i,j)}$ for all (i, j) in the image and C as the set of all color pixels $c_{(i,j)}$ for all (i, j) in the image, $i = 1, \dots, N_R$, $j = 1, \dots, N_C$ with N_R the number of rows, and N_C the number columns in the image. Since $X_{(i,j)}$ and $c_{(i,j)}$ are vectors, H and C can be expressed as

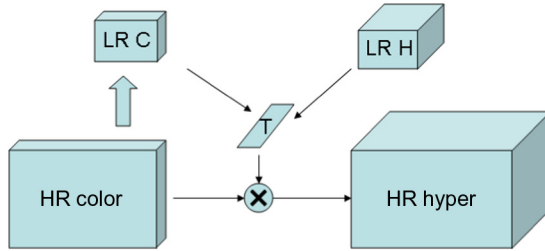


Fig. 1 System flow of color mapping. LR denotes low resolution; HR denotes high resolution; LR C denotes the set of low-resolution color pixels; LR H denotes the set of low-resolution hyperspectral pixels; HR Hyper denotes high-resolution hyperspectral pixels.

$$H = [X_{(1,1)} \quad X_{(1,2)} \quad \dots \quad X_{(N_R, N_C)}], \quad C = [C_{(1,1)} \quad C_{(1,2)} \quad \dots \quad C_{(N_R, N_C)}].$$

We call Eq. (1) the global version and all pixels in C and H are used in estimating T . To estimate T , we will use the least squares approach, which minimizes the error

$$E = \sum_{i=1}^{N_R} \sum_{j=1}^{N_C} \left[X_{(i,j)} - T c_{(i,j)} \right]^{\text{Transpose}} \left[X_{(i,j)} - T c_{(i,j)} \right]. \quad (2)$$

Following the definition of Frobenius norm,⁴⁰ Eq. (2) is equivalent to

$$E = \|H - TC\|_F^2. \quad (3)$$

Solving T in Eq. (3) involves the following. Since

$$\begin{aligned} E &= \|H - TC\|_F^2 = \text{tr}[(H - TC)(H - TC)^T] \\ &= \text{tr}[HH^T] - \text{tr}[HC^TT^T] - \text{tr}[TCH^T] + \text{tr}[TCC^TT^T]. \end{aligned} \quad (4)$$

Differentiating Eq. (4) with respect to T yields⁴¹

$$\frac{\partial E}{\partial T} = -2HC^T + 2TCC^T.$$

Setting the above to zero will yield

$$T^* = HC^T(CC^T)^{-1}. \quad (5)$$

Unlike normal image mapping such as the 3×3 image transform matrices (a rotation or perspective transformation), which maps between spatially distributed patches, it should be noted that T is a pixel to pixel mapping between color pixels and hyperspectral pixels.

To avoid instability, we can add a regularization term in Eq. (3). That is,

$$T^* = \arg \min_T \|H - TC\|_F + \lambda \|T\|_F. \quad (6)$$

And the optimal T becomes

$$T^* = HC^T(CC^T + \lambda I)^{-1}, \quad (7)$$

where λ is a regularization parameter and I is an identity matrix with the same dimension as CC^T .

2.2 Hybrid Color Mapping

For many hyperspectral images, the band wavelengths range from 0.4 to 2.5 μm . For color images, the R , G and B wavelengths are 0.65, 0.51, and 0.475 μm , respectively. Therefore, the three color bands may have little correlation with higher number bands in the hyperspectral

image. To mitigate this issue, we extract several higher number bands from the LR hyperspectral image and stack them with LR color bands. This is illustrated in Fig. 2. To be more specific, for a given pixel c with $c = [c(1), \dots, c(M)]^T$ in the original LR color image, a new color pixel known as hybrid color pixel c_h is created as

$$c_h = [c(1), \dots, c(M), h(k_1), h(k_2), \dots, h(k_t), 1]^T, \quad (8)$$

where $[h(k_1), h(k_2), \dots, h(k_t)]$ are extracted from the LR hyperspectral image. k_t is the number of selected bands. The selected bands from the LR hyperspectral image are used to increase correlation for the mapping. In the extreme case, if we pick all hyperspectral image bands and no color image bands, then the process is the same as bicubic upsampling. The number of selected bands k_t is a design parameter and is data dependent. Thus, this hybrid mapping is similar to the fusion of bicubic upsampling and pure color mapping. In addition to the higher number image bands, we also add a white band, i.e., all pixel values are 1. This white band can be used to compensate for the atmospheric effect and other bias effects. Mathematically, adding a white band is equivalent to adding one more column in the T matrix. Hence, we have more parameters to adjust in the transformation. Consequently, the mapping will be even more accurate.

Using the same treatment in Sec. 2.1, T can be obtained by minimizing the mean square error

$$T^* = \arg \min_T \|H - TC_h\|_F,$$

where H is the set of hyperspectral pixels and C_h is the set of hybrid color pixels. All the pixels in H and C_h are used. The optimal T can be determined as

$$T^* = HC_h^T(C_h C_h^T)^{-1}. \quad (9)$$

With regularization, Eq. (9) becomes

$$T^* = HC_h^T(C_h C_h^T + \lambda I)^{-1}. \quad (10)$$

2.3 Local Hybrid Color Mapping

We further enhance our method by applying color mapping patch by patch. A patch of size $p \times p$ is a subimage in the original image. The patches do not overlap. Each patch will have a unique local transformation matrix, T_i , $i = 1, \dots, P$ with P the total number of patches in the LR color and LR hyperspectral images. Mathematically, Eqs. (5), (7), (9), and (10), respectively, become

$$\begin{aligned} T_i^* &= H_i C_i^T (C_i C_i^T)^{-1}, & T_i^* &= H_i C_i^T (C_i C_i^T + \lambda I)^{-1}, \\ T_i^* &= H_i C_{hi}^T (C_{hi} C_{hi}^T)^{-1}, & T_i^* &= H_i C_{hi}^T (C_{hi} C_{hi}^T + \lambda I)^{-1}, \end{aligned}$$

where H_i contains p^2 hyperspectral pixels of dimension R^N , C_i contains p^2 color pixels of dimension R^M , and C_{hi} contains p^2 color pixels of dimension R^{M+k_t+1} . It is understood that the dimension of I 's in the above equations have varying dimensions accordingly.

In this way, spatial correlation can be exploited. As a result, the mapping will be even more accurate. In addition, since the task is split into many small tasks, the process can be easily parallelized and hence is suitable for real-time processing.

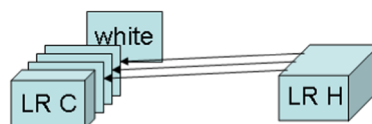


Fig. 2 System flow of HCM.

3 Comparative Studies

We used two hyperspectral image datasets in our experiments. One was from the AF (for short) and one was from NASA. The one from NASA is actually an AVIRIS image. The AF image^{15–16} has 124 bands ranging from 461 to 901 nm. The AVIRIS image has 213 bands with wavelengths from 380 to 2500 nm. Figure 3 shows a sample band of both datasets. Both of them are natural scenes. The AF image size is $267 \times 342 \times 124$ pixels and the AVIRIS image size is $300 \times 300 \times 213$ pixels.

In each experiment, we downsampled the image by three times using a 5×5 Gaussian kernel. This is a common practice in pansharpening.³⁷ The blurred and downsampled image was used as the LR hyperspectral image that needs to be improved. We picked *R*, *G*, *B* bands from the original HR hyperspectral image for color mapping.

3.1 Comparison with State-of-the-Art Hyperspectral Pansharpening Algorithms

In the paper by Loncan et al.,³⁷ about 10 hyperspectral pansharpening algorithms were divided into four groups: component substitution, multiresolution analysis, hybrid methods, and Bayesian-based methods. We took a different angle in this paper. We divide the pansharpening methods into three groups. Group 1 contains methods that require multispectral bands and sensor characteristics such as PSF. In this group, there are three methods, which are known as coupled nonnegative matrix factorization (CNMF),³⁴ Bayesian naïve,³⁵ and Bayesian sparse.³⁶ These methods can directly fuse HR multispectral bands with LR hyperspectral bands. PSF is also needed in these methods. Group 2 contains methods that do not require sensor characteristics, but require a pan band. Our HCM method is similar to Group 2 methods in that we do not require PSF. The following methods have been included in Group 2: smoothing filter-based intensity modulation (SFIM),³⁸ modulation transfer function generalized Laplacian pyramid (MTF-GLP),³⁰ MTF-GLP with high-pass modulation (MTF-GLP-HPM),³¹ Gram schmidt (GS),²⁸ GS adaptive (GSA),²⁹ principal component analysis (PCA),²⁶ guided filter PCA (GFPICA),²⁷ Hysure,^{32,33} and variational wavelet pansharpening (VWP).^{25,42} VWP^{25,42} was not included in Ref. 37. However, since we have already implemented VWP, we included it in Group 2. Finally, the methods in Group 3 do not require multispectral bands or PSF. Two representative methods, SR⁴³ and bicubic interpolation,⁴⁴ are included here.

3.1.1 Performance metrics

Similar to Ref. 37, five performance metrics are included here.

Time: This is the computational time in seconds. This metric is machine dependent and varies with runs. However, it gives a relative measure of the computational complexity of different algorithms.

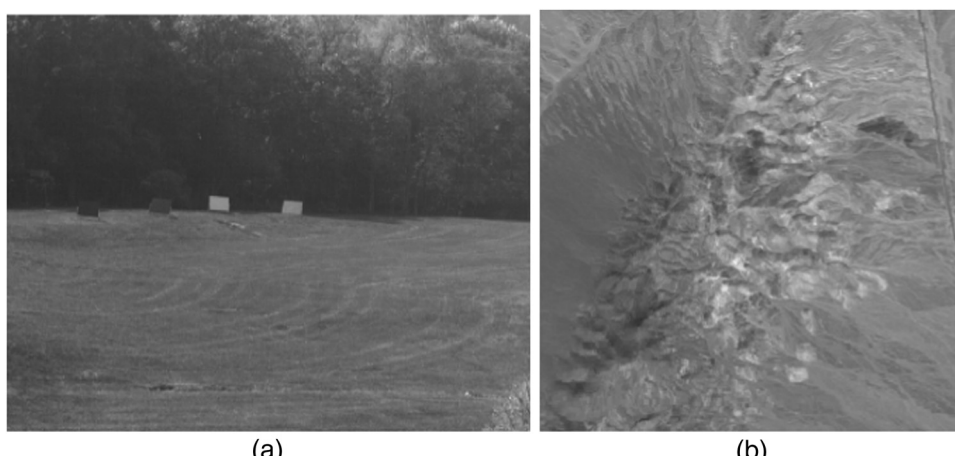


Fig. 3 (a) Sample band from AF data and (b) Sample band from AVIRIS data.

*Root-mean-squared error (RMSE):*³⁷ Given two matrices X and \hat{X} , the RMSE is calculated by using

$$\text{RMSE}(X, \hat{X}) = \frac{\|X - \hat{X}\|_F}{\sqrt{\text{total number of pixels}}}.$$

The ideal value of RMSE is 0. Since RMSE is a scalar, it does not reveal the RMSE values at different bands. Therefore, we also used $\text{RMSE}(\lambda)$ which is the RMSE value between $X(\lambda)$ and $\hat{X}(\lambda)$ for each band λ , to evaluate the performance of different algorithms.

*Cross correlation (CC):*³⁷ It is defined as

$$\text{CC}(X, \hat{X}) = \frac{1}{m_\lambda} \sum_{i=1}^{m_\lambda} \text{CCS}(X^i, \hat{X}^i),$$

where m_λ is the number of bands in the hyperspectral image and CCS is the cross correlation for a single-band image, given by

Table 1 Comparison of HCM with all methods in Group 1 using the AF image.

Method	Time	RMSE	CC	SAM	ERGAS
CNMF ³⁴	12.52254	0.59917	0.99218	1.4351	1.7229
Bayes naïve ³⁵	0.575655	0.43573	0.98807	1.2141	1.6588
Bayes sparse ³⁶	208.82	0.41329	0.99003	1.2395	1.5529
HCM	0.586851	0.58121	0.99075	1.4223	1.751

Table 2 Comparison of HCM with all methods in Group 1 using the AVIRIS image.

Method	Time	RMSE	CC	SAM	ERGAS
CNMF ³⁴	23.74715	32.2868	0.94558	0.95904	2.1225
Bayes naïve ³⁵	0.860668	67.2879	0.94738	0.81362	2.1078
Bayes sparse ³⁶	235.4995	51.701	0.96188	0.76349	1.8657
HCM	3.563552	41.931	0.9501	0.9954	2.0155

Table 3 Comparison of HCM with all methods in Group 3 using the AF image.

Method	Time	RMSE	CC	SAM	ERGAS
SR ⁴³	279.1789	0.52315	0.98386	1.3215	1.9584
Bicubic ⁴⁴	0.041152	0.58524	0.98066	1.3554	2.156
HCM	0.586851	0.58121	0.99075	1.4223	1.751

Table 4 Comparison of HCM with all methods in Group 3 using the AVIRIS image.

Method	Time	RMSE	CC	SAM	ERGAS
SR ⁴³	1329.592	86.7154	0.92634	0.99697	2.411
Bicubic ⁴⁴	0.10378	92.2143	0.91179	1.0369	2.5728
HCM	3.563552	41.931	0.9501	0.9954	2.0155

Table 5 Comparison of HCM with all methods in Group 2 using the AF image.

Method	Time	RMSE	CC	SAM	ERGAS
SFIM ³⁸	3.677398	0.6324	0.99006	1.3449	1.8881
MTF GLP ³⁰	5.806203	0.74201	0.98817	1.4738	2.1628
MTF GLP HPM ³¹	5.802082	0.7255	0.98866	1.402	2.1171
GS ²⁸	3.457196	2.166	0.85896	2.35	7.0568
GSA ²⁹	3.821432	0.65721	0.98955	1.3541	1.9617
PCA ²⁶	9.95679	2.3755	0.8387	2.549	7.7105
GPCA ²⁷	6.377541	0.67542	0.98373	1.5688	2.1893
Hysure ^{32,33}	144.95	0.81009	0.98323	1.6748	2.4467
VWP ²⁵	6665.764	0.64561	0.98844	1.3904	2.0722
HCM	0.577121	0.58121	0.99075	1.4223	1.751

Table 6 Comparison of HCM with all methods in Group 2 using the AVIRIS image.

Method	Time	RMSE	CC	SAM	ERGAS
SFIM ³⁸	1.532656	37.0572	0.97366	0.72048	1.5931
MTF GLP ³⁰	2.131287	26.4199	0.97715	0.69747	1.5132
MTF GLP HPM ³¹	2.136418	26.5246	0.97715	0.69688	1.5159
GS ²⁸	1.638365	54.161	0.96241	0.83237	1.8748
GSA ²⁹	2.001172	42.8342	0.9698	0.76857	1.6734
PCA ²⁶	2.970278	48.0821	0.968	0.81085	1.7678
GPCA ²⁷	1.935442	73.6587	0.93617	1.2344	2.4518
Hysure ^{32,33}	66.08687	38.8677	0.95439	1.0355	1.9516
VWP ²⁵	7046.138	129.2581	0.78448	3.2882	14.14412
HCM	3.563552	41.931	0.9501	0.9954	2.0155

$$\text{CCS}(A, B) = \frac{\sum_{j=1}^n (A_j - \mu_A)(B_j - \mu_B)}{\sqrt{\sum_{j=1}^n (A_j - \mu_A)^2 \sum_{j=1}^n (B_j - \mu_B)^2}}.$$

The ideal value of CC is 1. We also used $\text{CC}(\lambda) = \text{CCS}(X^i, \hat{X}^i)$, which is the CC value between $X(\lambda)$ and $\hat{X}(\lambda)$ for each band, to evaluate the performance of different algorithms.

Spectral angle mapper (SAM):³⁷ It is defined as

$$\text{SAM}(X, \hat{X}) = \frac{1}{n} \sum_{j=1}^n \text{SAM}(x_j, \hat{x}_j),$$

where for two vectors $a, b \in R^{m_\lambda}$,

$$\text{SAM}(a, b) = \arccos\left(\frac{\langle a, b \rangle}{\|a\|\|b\|}\right),$$

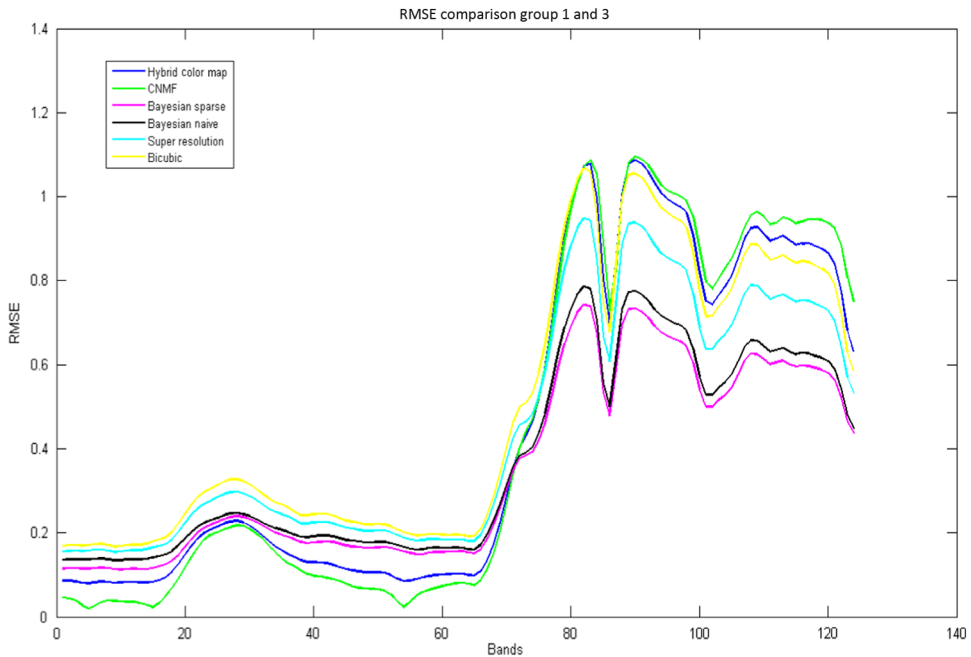


Fig. 4 Comparison of RMSE between HCM and all methods in Groups 1 and 3 using AF image.

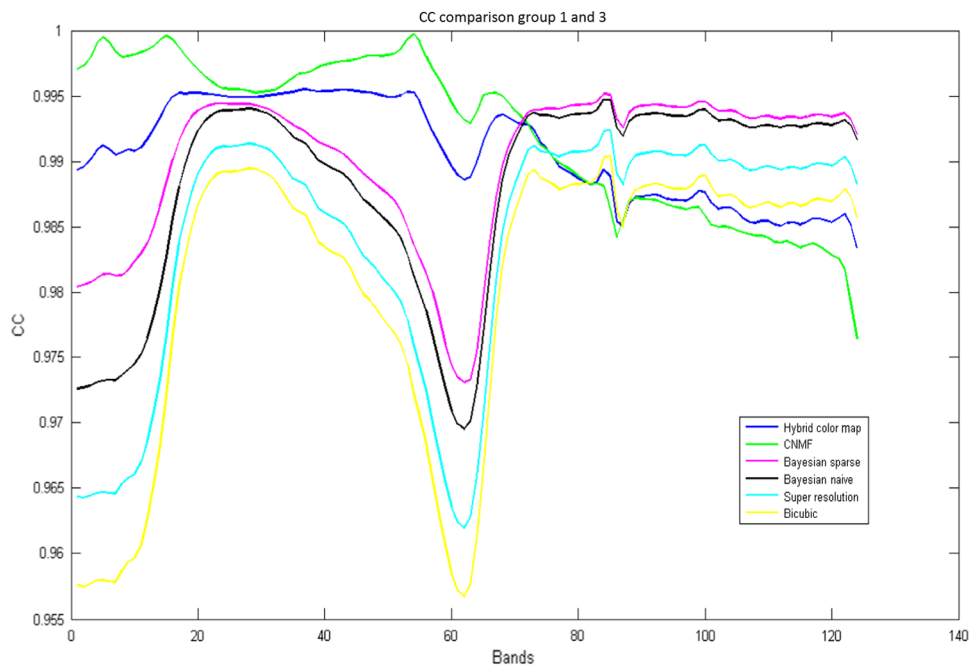


Fig. 5 Comparison of RMSE between HCM and all methods in Groups 1 and 3 using AVIRIS image.

$\langle a, b \rangle$ is the inner product between two vectors and $\| \cdot \|$ denotes the 2-norm of a vector. The ideal value of SAM is 0.

*Erreur relative globale adimensionnelle de synthèse (ERGAS):*³⁷ It is defined as

$$\text{ERGAS}(X, \hat{X}) = 100d \sqrt{\frac{1}{m_\lambda} \sum_{k=1}^{m_\lambda} \left(\frac{\text{RMSE}_k}{\mu_k} \right)^2},$$

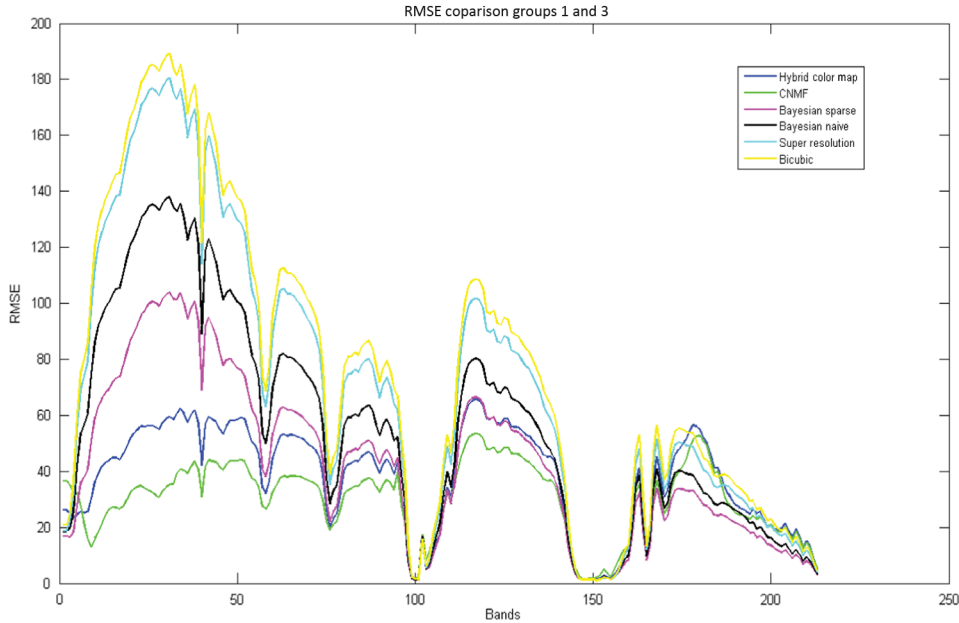


Fig. 6 Comparison of CC between HCM and all methods in Groups 1 and 3 using AF image.

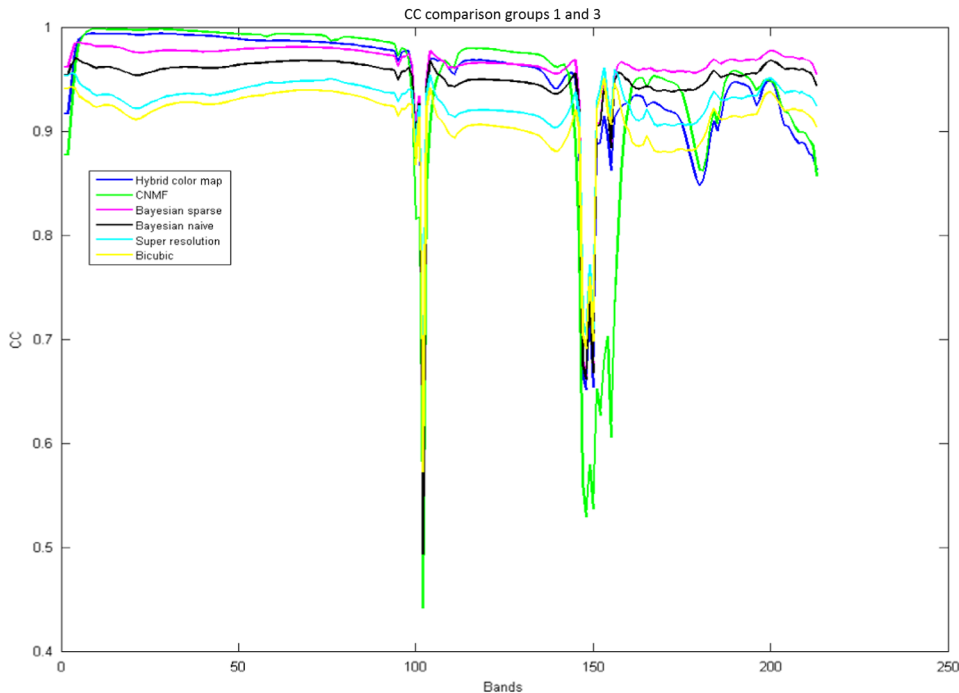


Fig. 7 Comparison of CC between HCM and all methods in Groups 1 and 3 using AVIRIS image.

where d is the ratio between the linear resolutions of the PAN and HS images, defined by

$$d = \frac{\text{PAN linear spatial resolution}}{\text{HS linear spatial resolution}},$$

where μ_k is the sample mean of the k 'th band of X . The ideal value of ERGAS is 0.

3.1.2 Comparison of HCM with methods in Groups 1 and 3

The comparisons of our HCM with others in Groups 1 to 3 are shown in Tables 1–6. To save some space, we present some performance plots by combining the results of all methods from Groups 1

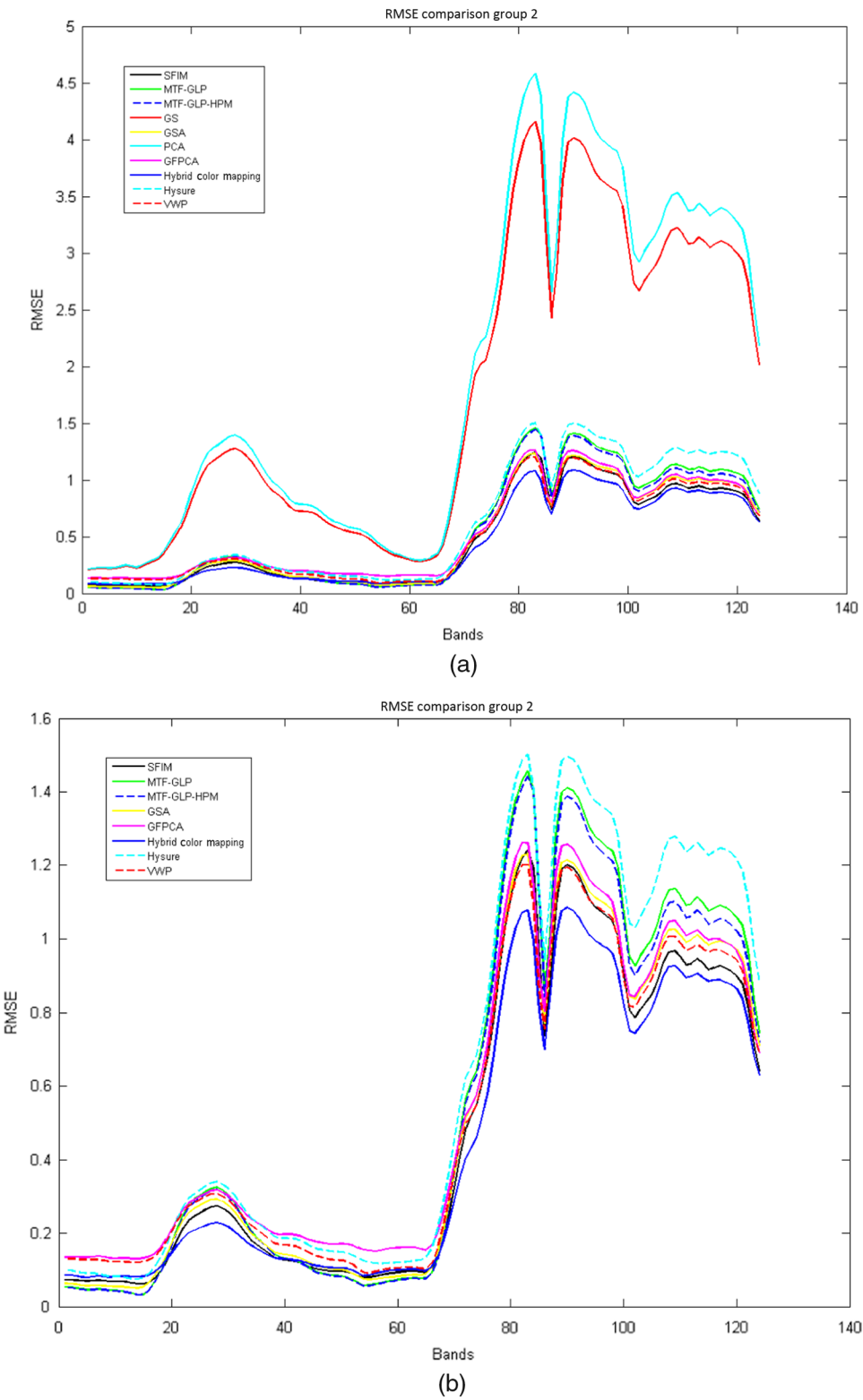


Fig. 8 Comparison of RMSE between HCM and all methods in Group 2 using AF image. (a) All methods in Group 2 and (b) results without PCA and GS.

and 3. Both AF and NASA AVIRIS images were used in this study. In all of our experiments, we used local HCM, where 7×7 pixel patches were used. We experimented with the number (k_t) of LR hyperspectral bands in the hybrid color pixel. It turns out that the best compromise is the case where we did not use any of the LR bands for the given downscaling factor.

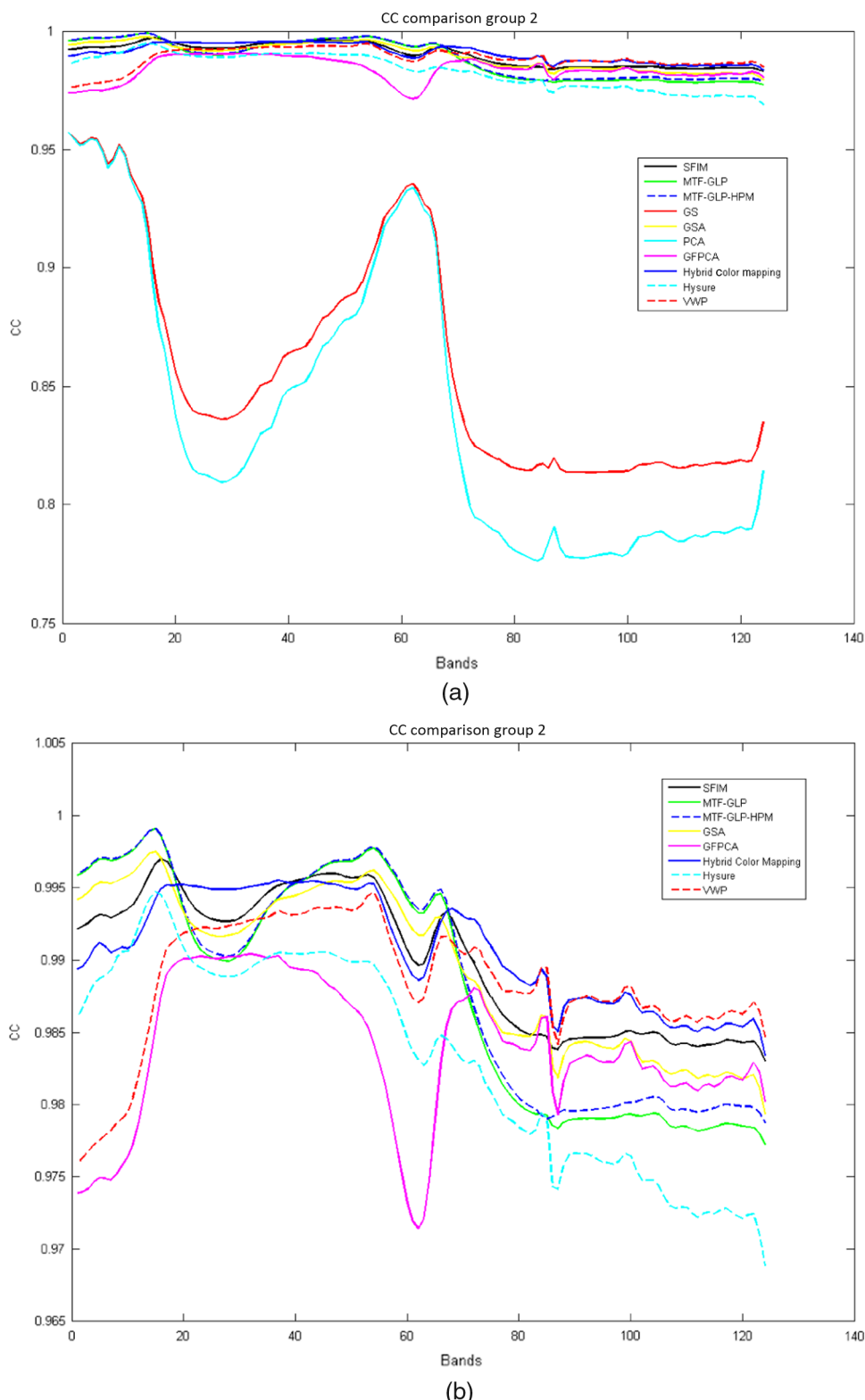


Fig. 9 Comparison of CC between HCM and all methods in Group 2 using AF image. (a) All methods in Group 2 and (b) results without PCA and GS.

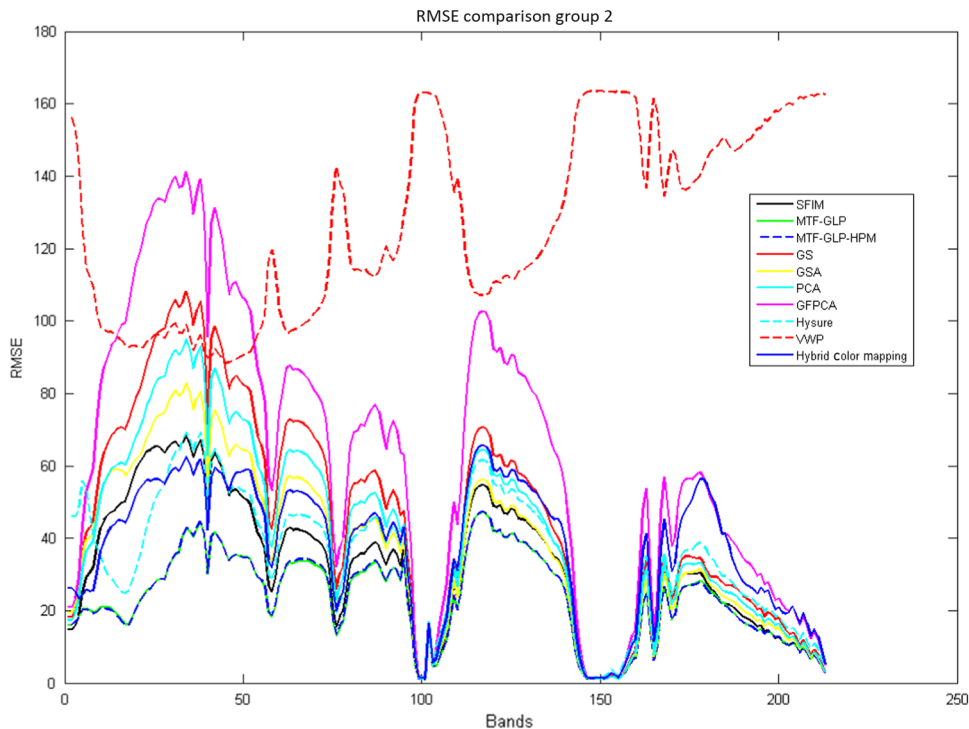


Fig. 10 Comparison of RMSE between HCM and all methods in Group 2 using AVIRIS image.

Comparison with methods in Group 1 (coupled nonnegative matrix factorization, Bayesian naïve, and Bayesian sparse). It should be noted that Group 1 methods (CNMF,³⁴ Bayesian naïve,³⁵ and Bayesian sparse³⁶) require PSF information, whereas our HCM algorithm does not. From Table 3, it can be seen that none of the methods can outperform the others. The performance of HCM is fast in terms of speed. In terms of RMSE, CC, SAM, and ERGAS, HCM is comparable to CNMF. From the RMSE plot shown in Fig. 4, it can be seen that HCM performed quite well in bands up to 65 for the AF image. Actually, HCM is better than Bayesian naïve and Bayesian sparse in bands <65. Also, from the RMSE plot shown in Fig. 5 for the AVIRIS data, HCM performed better than Bayesian sparse up to band 100, and better than Bayesian naïve up to band 150. From Table 4, it can be seen that HCM is also comparable to CNMF in terms of CC, SAM, and ERGAS. In terms of RMSE, HCM performed better than Bayesian naïve and Bayesian sparse. From the CC plot shown in Fig. 6 for the AF data, we can see that HCM performed well quite consistently across all bands, whereas CNMF, Bayesian naïve, and Bayesian sparse all have large fluctuations across the bands. Also, from the CC plot shown in Fig. 7, HCM performed better than both Bayesian naïve and Bayesian sparse up to band 100, better than Bayesian naïve up to band 150, and comparable to CNMF in bands beyond 150. We cannot plot SAM and ERGAS as these two metrics are scalars.

Given the fact that our HCM algorithm does not require PSF information and can still achieve a comparable or better performance in some situations than those computationally intensive methods in Group 1, this clearly shows that HCM is among the top performers.

Comparison with methods in Group 3 (super-resolution and bicubic). From Table 3 for the AF image, it can be seen that HCM performed better than SR⁴³ in terms of computational time, CC, and ERGAS. HCM also performed better than bicubic⁴⁴ in terms of RMSE, CC, and ERGAS. From Table 4 for the AVIRIS image, it is clear to see that HCM performed better than SR and bicubic in terms of RMSE, CC, SAM, and ERGAS. From Figs. 4–7, one can see that HCM performed better than SR and bicubic in most bands.

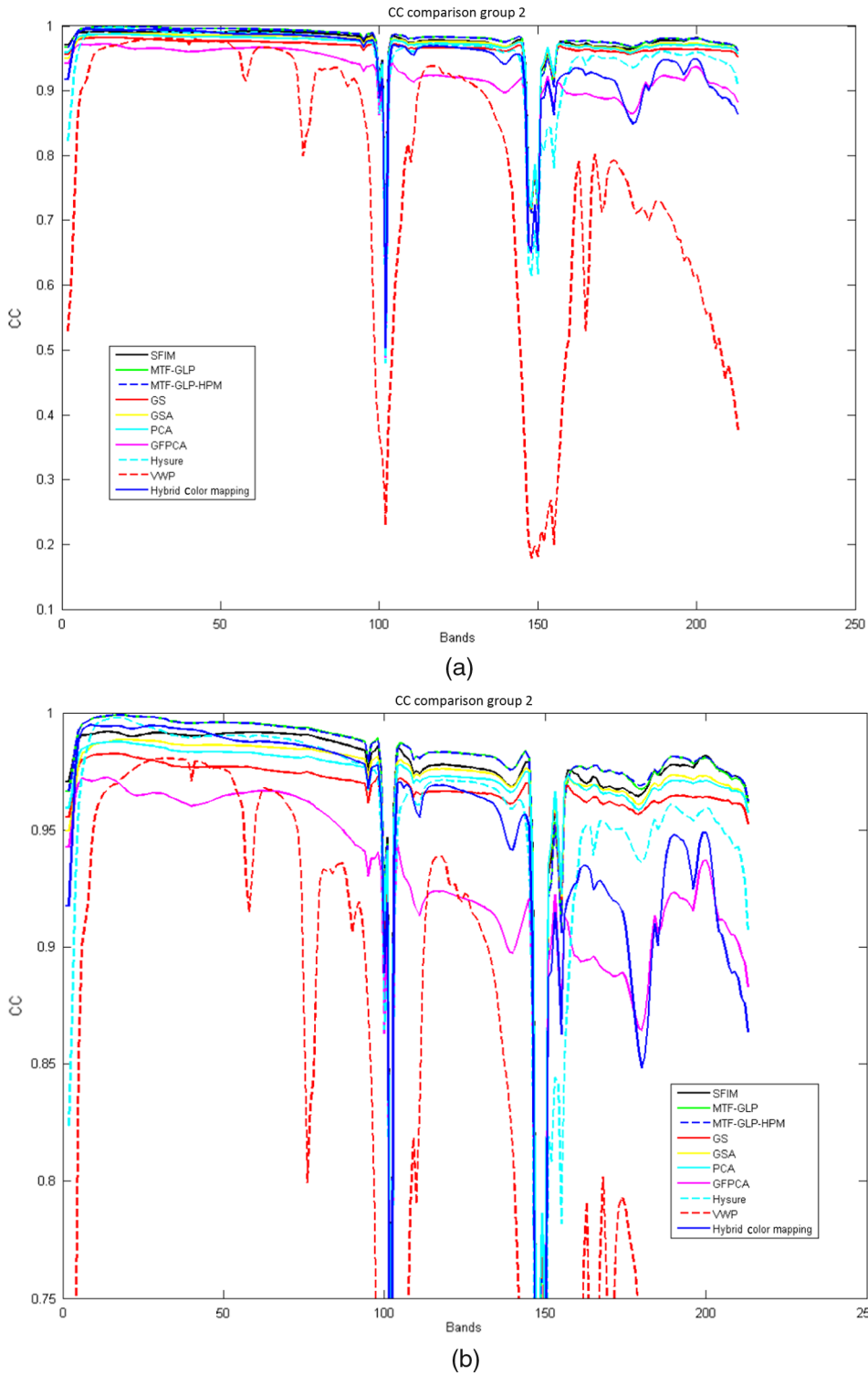
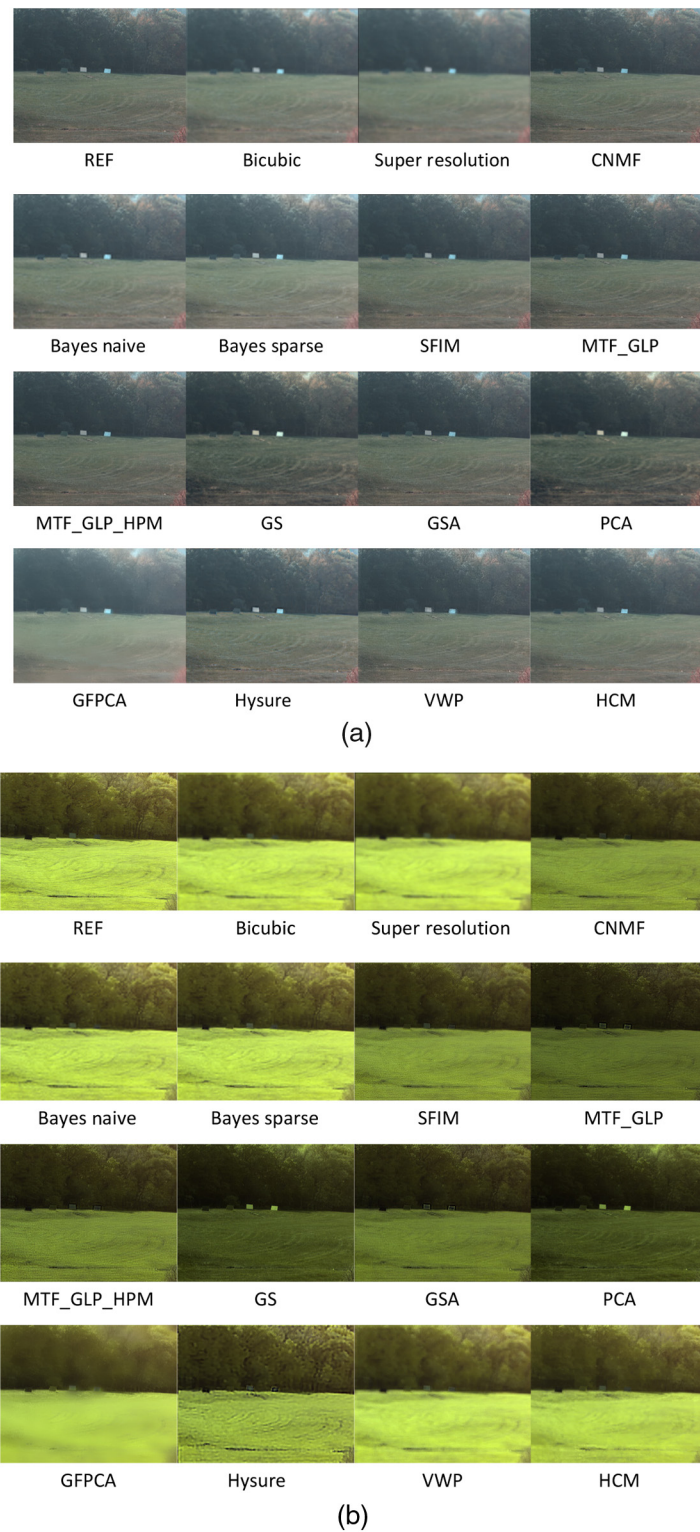


Fig. 11 Comparison of CC between HCM and all methods in Group 2 using AVIRIS image. (a) All methods in Group 2 and (b) Zoomed in plot of (a).

3.1.3 Comparison with methods in Group 2

Since our proposed HCM algorithm does not require PSF, it will be fair to compare it with those algorithms that do not require PSF. Methods in Group 2 satisfy the above criterion. The methods in Group 2 require a pan band that was created by taking the mean of the *R*, *G*, *B* bands. From Table 5 (AF data), HCM achieved the best in four out of five categories. From Figs. 8 and 9, it

**Fig. 12** Fused AF images using different methods. (a) Visible range and (b) VNIR range.

can be seen that HCM performed consistently well across all bands as compared to other methods. As shown in Table 6 for the AVIRIS data, although HCM was not the top performer, it performed better than or comparable to those highly time consuming methods such as Hysure and VWP. In Figs. 10 and 11, HCM is comparable to those top performers in bands up to 150.

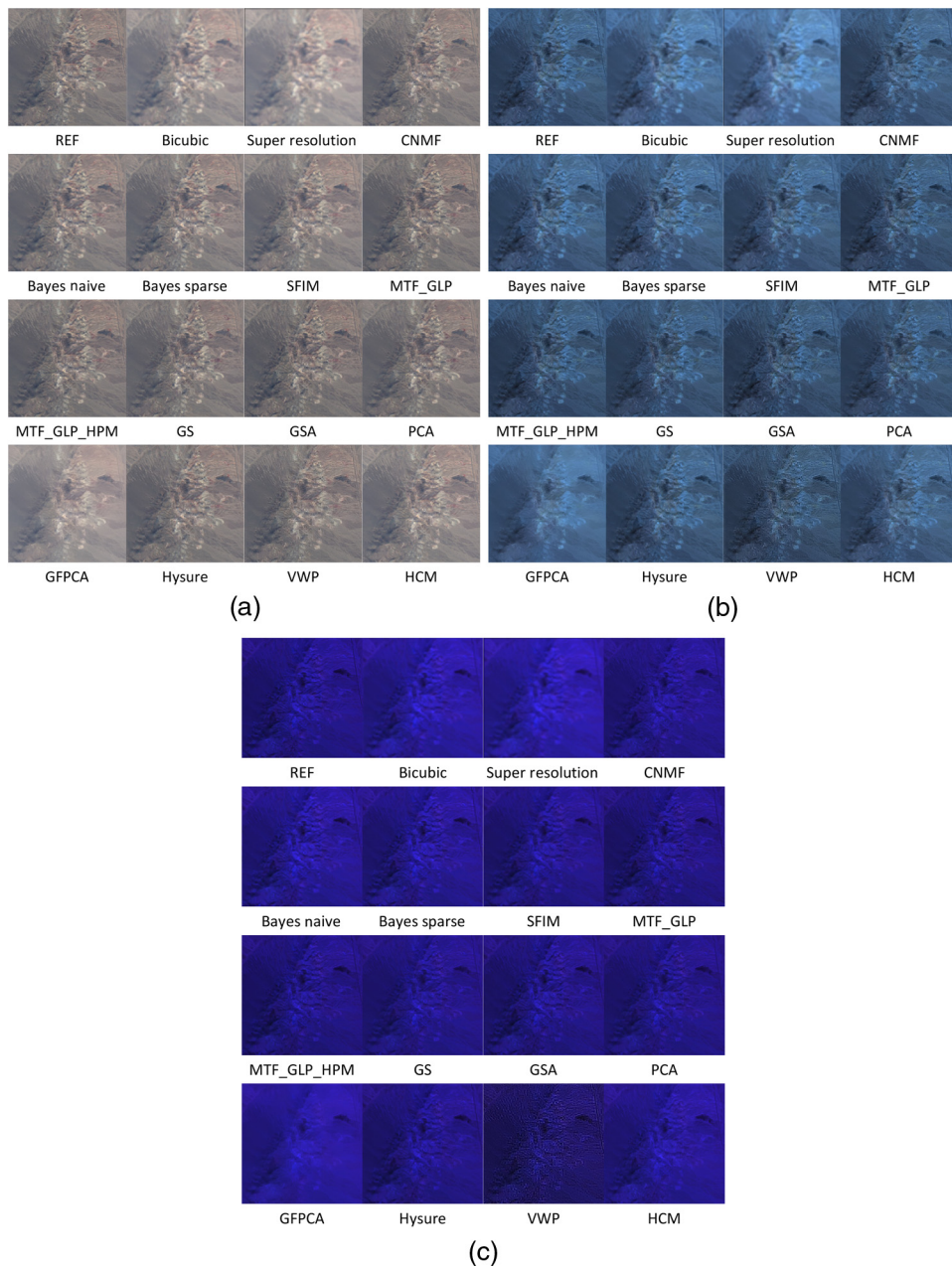


Fig. 13 Fused AVIRIS images using different methods. (a) Visible range, (b) VNIR range, and (c) SWIR range.

3.2 Visualization of Fused Images Using Different Methods

Here, we present a subjective comparison of fused images using HCM and all methods mentioned in Groups 1 to 3. Figure 12 shows the synthesized color images from the fused AF hyperspectral image in visible range using bands (5, 15, 54) and VNIR (visible near-infrared) range using bands (70, 90, 110), respectively. HCM can be seen to preserve spectral fidelity quite well. Some methods such as CNMF, GS, PCA, SFIM, and so on clearly have strong spectral distortions in the VNIR range. For completeness, we also include the synthesized color images in three spectral ranges of the fused AVIRIS image in Fig. 13. However, it is somewhat hard to see the subtle differences between different methods. For AVIRIS data, the visible, VNIR, and SWIR (short-wave infrared) images are formed by using bands (9, 18, 27), (50, 70, 90), and (120, 160, 200), respectively.

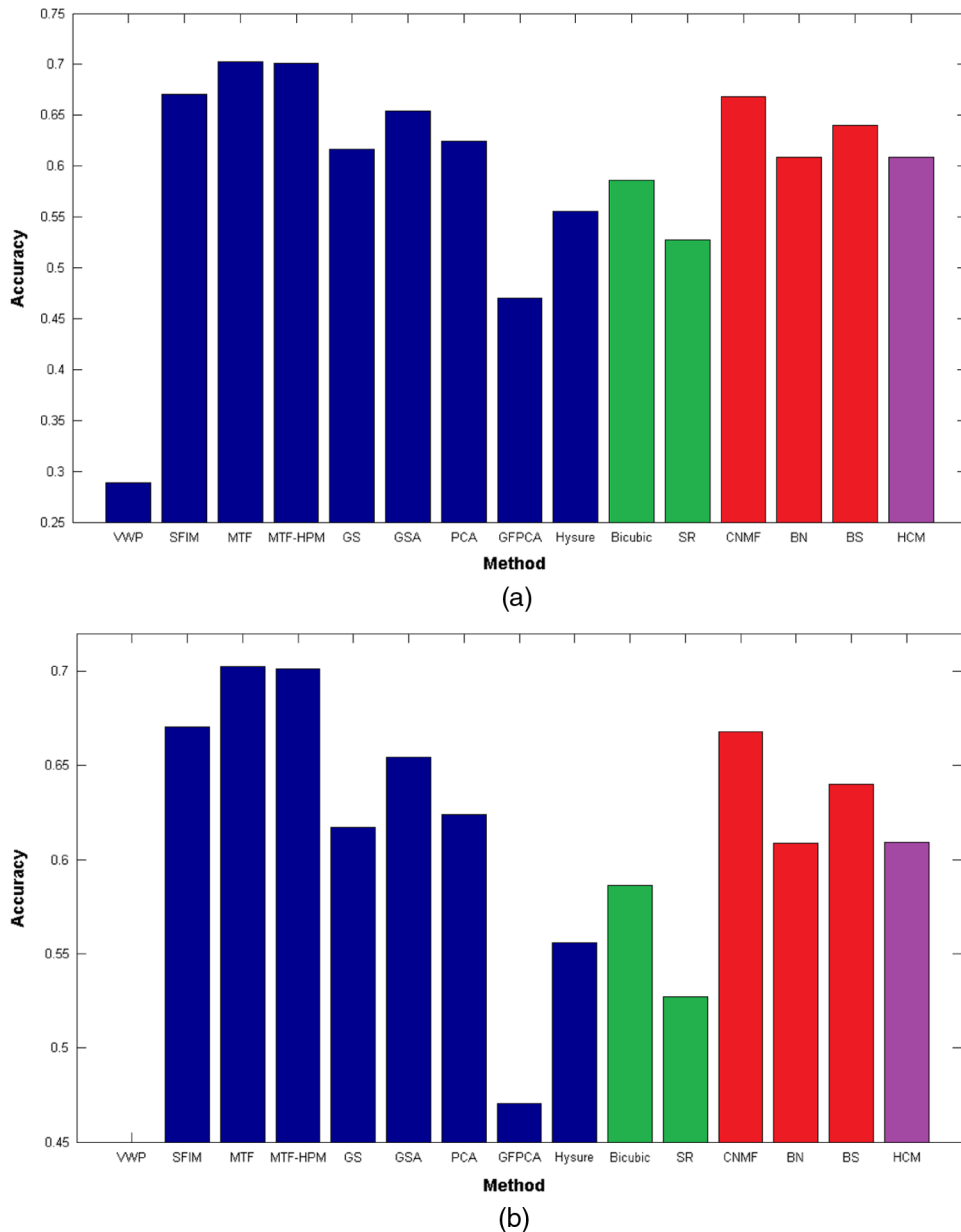


Fig. 14 Classification accuracy using different methods. Group 1 methods are in red; Group 2 methods are in blue; Group 3 methods are in green; HCM is in purple. (a) Results of all methods and (b) zoomed in results of (a).

3.3 Classification Enhancement Using the SR Images

In addition to those objective and subjective evaluations in the above two sections, we also performed another investigation, as the goal of our research is not only to improve the visual performance of the hyperspectral images by enhancing the spatial resolution, but also to enhance the target classification performance as well. Figure 14 shows classification results using different methods based on endmembers extracted from the ground truth AVIRIS hyperspectral image. We used the *K*-means endmember extraction technique to determine the endmembers. Classification was done by using SAM. It can be seen that HCM produced comparable results as some of the high-performance methods as shown in Fig. 14. One observation is that bicubic interpolation produced a reasonable performance. Another observation is that the MTF-GLP based methods performed quite well in this study. From the study in Ref. 37, it was observed that the Bayesian sparse algorithm performed consistently well. However, the MTF-GLP method

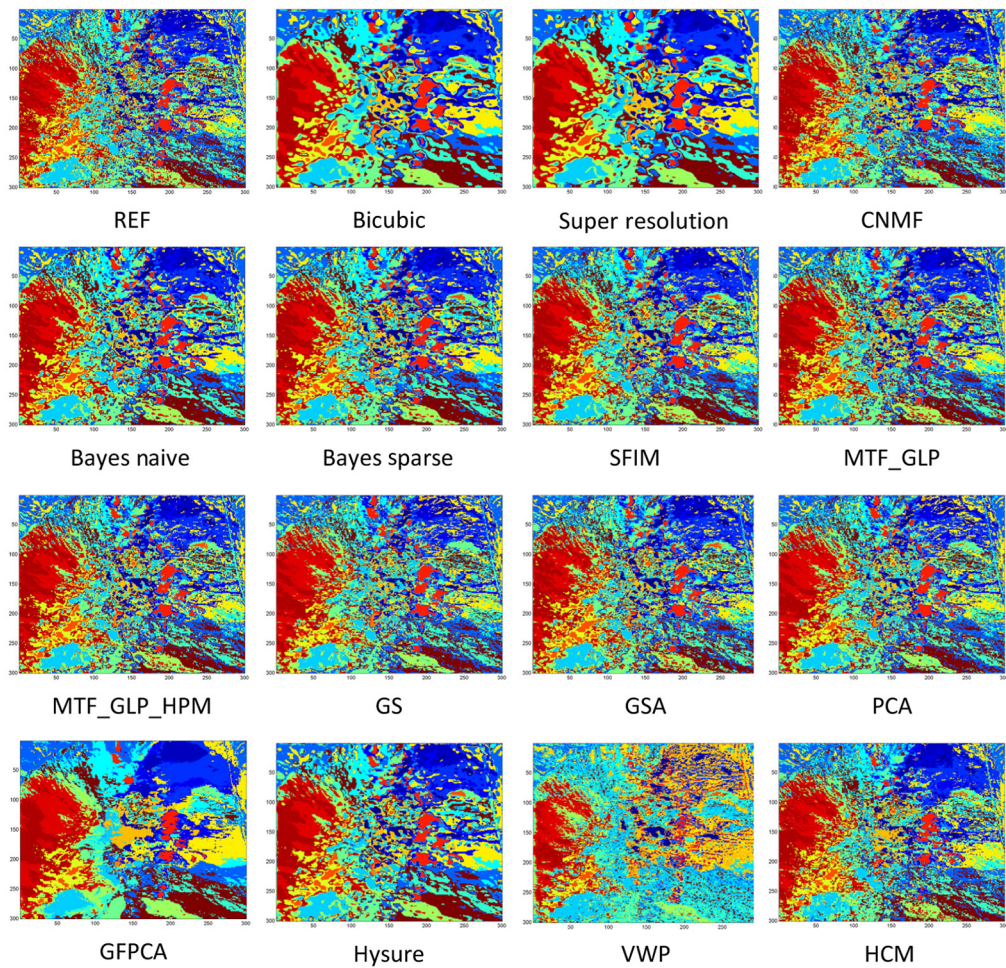


Fig. 15 Comparison of classification maps using different methods.

is comparable to or better than Bayesian sparse for the AVIRIS data. This means that the performance of pansharpening is data dependent and it is worth experimenting with different algorithms for a new application. The classification maps are shown in Fig. 15. It can be seen that classification maps from the top performers can be seen to be closer to the reference map (ground truth).

4 Conclusions

In this paper, we proposed a HCM SR algorithm for hyperspectral images. The idea is to fuse a high spatial resolution RGB image or multispectral image with a low spatial resolution hyperspectral image to produce a high spatial resolution hyperspectral image. Extensive comparative studies with >10 state-of-the-art algorithms have been carried out using actual data. Five performance metrics were used in our experiments. Experiments showed that the proposed HCM method is better than or comparable to some of the top performers, especially those Group 2 methods that do not require PSF. It should be emphasized that our HCM also does not require PSF. It is also shown that using the reconstructed images, classification performance can be improved quite significantly by some of the top performers in this study. High spatial resolution hyperspectral imaging is a fundamental requirement for many applications such as mineral mapping, search and rescue missions, and others. We believe our technique as well as those top performers in this study will have a great impact in all future HyspIRI applications.¹ One key advantage of our technique is that it is very efficient and can be easily parallelized. In our experiments, we noticed that our HCM is comparable to some high-performance algorithms

in terms of four out of five objective metrics, but with much lower computational complexity. It is, therefore, suitable for real-time applications.

Future work will include the packaging of our algorithm as well as some of the top performers in this study into some NASA data products.

Acknowledgments

This research was funded by NASA under contract # NNX12CE41P. Any opinions, findings, and conclusions or recommendations expressed in this material are those of the author(s) and do not necessarily reflect the views of NASA. We would like to thank the reviewers for their detailed comments and suggestions, which significantly improved the quality and readability of this paper. Technical discussions with Ms. L. Loncan and Dr. Q. Wei related to the open source codes in the openremotesensing.net website were tremendously helpful in running our simulations. We also would like to thank the authors of Ref. 43 for sharing their source codes with us.

References

1. C. M. Lee et al., “An introduction to the NASA hyperspectral infrared imager (HyspIRI) mission and preparatory activities,” *Remote Sens. Environ.* **167**, 6–19 (2015).
2. J. Zhou et al., “A high performance algorithm to improve the spatial resolution of HyspIRI images,” in *NASA HyspIRI Science and Applications Workshop*, Washington, D.C. (2012).
3. C. Kwan et al., “Fast parallel processing tools for future HyspIRI data processing,” in *NASA HyspIRI Science Symp.*, Greenbelt, Maryland (2013).
4. B. Ayhan and C. Kwan, “Fast target detection framework for onboard processing of multispectral and hyperspectral images,” in *HyspIRI Science Symp.*, Greenbelt, Maryland (2015).
5. J. Zhou, C. Kwan, and B. Ayhan, “A high performance missing pixel reconstruction algorithm for hyperspectral images,” in *2nd Int. Conf. on Applied and Theoretical Information Systems Research*, Taipei, Taiwan (2012).
6. D. Nguyen et al., “Endmember extraction in hyperspectral images using l_1 minimization and linear complementary programming,” *Proc. SPIE* **7695**, 76951M (2010).
7. J. Zhou, C. Kwan, and B. Ayhan, “Hybrid in-scene atmospheric compensation (H-ISAC) of hyperspectral images for high performance target detection,” in *Int. Symp. on Spectral Sensing Research*, Missouri (2010).
8. H. Kwon and N. M. Nasrabadi, “Kernel RX-algorithm: a nonlinear anomaly detector for hyperspectral imagery,” *IEEE Trans. Geosci. Remote Sens.* **43**(2), 388–397 (2005).
9. B. Ayhan et al., “Airborne detection of land mines using mid-wave infrared (MWIR) and laser-illuminated-near infrared images with the RXD hyperspectral anomaly detection method,” in *Fourth Int. Workshop on Pattern Recognition in Remote Sensing*, Hong Kong (2006).
10. L. He et al., “A comparative study of several unsupervised endmember extraction algorithms to anomaly detection in hyperspectral images,” in *Int. Symp. on Spectral Sensing Research*, Missouri (2010).
11. J. Zhou and C. Kwan, “Fast anomaly detection algorithms for hyperspectral images,” *J. Multidiscip. Eng. Sci. Technol.* **2**(9), 2521–2525 (2015).
12. W. Wang et al., “Identify anomaly component by sparsity and low rank,” in *IEEE Workshop on Hyperspectral Image and Signal Processing: Evolution in Remote Sensor (WHISPERS ‘15)*, Tokyo, Japan (2015).
13. S. Li et al., “Low-rank tensor decomposition based anomaly detection for hyperspectral imagery,” in *IEEE Int. Conf. on Image Processing (ICIP ‘15)*, Quebec City, Canada (2015).
14. B. Ayhan, J. Zhou, and C. Kwan, “High performance and accurate change detection system for HyspIRI missions,” in *NASA HyspIRI Science Symp.*, Greenbelt, Maryland (2012).
15. M. T. Eismann et al., “Hyperspectral change detection in the presence of diurnal and seasonal variations,” *IEEE Trans. Geosci. Remote Sens.* **46**(1), 237–249 (2008).
16. J. Zhou et al., “New and fast algorithms for anomaly and change detection in hyperspectral images,” in *Int. Symp. on Spectral Sensing Research*, Missouri (2010).

17. C.-I. Chang, *Hyperspectral Imaging: Techniques for Spectral Detection and Classification*, Kluwer Academic/Plenum Publishers, New York (2003).
18. T. Q. Pham, L. J. van Vliet, and K. Schutte, "Robust fusion of irregularly sampled data using adaptive normalized convolution," *EURASIP J. Appl. Signal Process.* **2006**, 083268 (2006).
19. S. Baker and T. Kanade, "Limits on super-resolution and how to break them," *IEEE Trans. Pattern Anal. Mach. Intell.* **24**(9), 1167–1183 (2002).
20. Z. Lin and H. Shum, "Fundamental limits of reconstruction-based superresolution algorithms under local translation," *IEEE Trans. Pattern Anal. Mach. Intell.* **26**(1), 83–97 (2004).
21. M. Elad, *Sparse and Redundant Representations*, Springer, New York (2010).
22. K. Kim and Y. Kwon, "Example-based learning for single-image SR and JPEG artifact removal," MPI-TR (173), Max Planck Institute for Biological Cybernetics, Germany (2008).
23. M. Choi, "A new intensity-hue-saturation fusion approach to image fusion with a tradeoff parameter," *IEEE Trans. Geosci. Remote Sens.* **44**, 1672–1682 (2006).
24. Q. Du et al., "On the performance evaluation of pan-sharpening techniques," *IEEE Geosci. Remote Sens. Lett.* **4**(4), 518–522 (2007).
25. M. Moeller et al., "A variational approach for sharpening high dimensional images," *SIAM J. Imag. Sci.* **5**(1), 150–178 (2012).
26. P. S. Chavez, Jr., S. C. Sides, and J. A. Anderson, "Comparison of three different methods to merge multiresolution and multispectral data: Landsat TM and SPOT panchromatic," *Photogramm. Eng. Remote Sens.* **57**(3), 295–303 (1991).
27. W. Liao et al., "Processing of multiresolution thermal hyperspectral and digital color data: Outcome of the 2014 IEEE GRSS data fusion contest," *IEEE J. Sel. Top. Appl. Earth Observations Remote Sensing* **8**(6), 2984–2996 (2015).
28. C. Laben and B. Brower, "Process for enhancing the spatial resolution of multispectral imagery using pan-sharpening," U.S. Patent 6 011 875 (2000).
29. B. Aiazzi, S. Baronti, and M. Selva, "Improving component substitution pansharpening through multivariate regression of MS + pan data," *IEEE Trans. Geosci. Remote Sens.* **45**(10), 3230–3239 (2007).
30. B. Aiazzi et al., "MTF-tailored multiscale fusion of high-resolution MS and pan imagery," *Photogramm. Eng. Remote Sens.* **72**(5), 591–596 (2006).
31. G. Vivone et al., "Contrast and error-based fusion schemes for multispectral image pan-sharpening," *IEEE Geosci. Remote Sens. Lett.* **11**(5), 930–934 (2014).
32. M. Simões et al., "A convex formulation for hyperspectral image superresolution via subspace-based regularization," *IEEE Trans. Geosci. Remote Sensing* **53**(6), 3373–3388 (2015).
33. M. Simões et al., "Hyperspectral image superresolution: an edge-preserving convex formulation," in *Proc. IEEE Int. Conf. Image Processing*, Paris, France, pp. 4166–4170 (2014).
34. N. Yokoya, T. Yairi, and A. Iwasaki, "Coupled nonnegative matrix factorization unmixing for hyperspectral and multispectral data fusion," *IEEE Trans. Geosci. Remote Sens.* **50**(2), 528–537 (2012).
35. R. C. Hardie, M. T. Eismann, and G. L. Wilson, "MAP estimation for hyperspectral image resolution enhancement using an auxiliary sensor," *IEEE Trans. Image Process.* **13**(9), 1174–1184 (2004).
36. Q. Wei et al., "Hyperspectral and multispectral image fusion based on a sparse representation," *IEEE Trans. Geosci. Remote Sens.* **53**(7), 3658–3668 (2015).
37. L. Loncan et al., "Hyperspectral pansharpening: a review," *IEEE Geosci. Remote Sens. Mag.* **3**(3), 27–46 (2015).
38. J. G. Liu, "Smoothing filter based intensity modulation: a spectral preserve image fusion technique for improving spatial details," *Int. J. Remote Sens.* **21**(18), 3461–3472 (2000).
39. B. Chen, "Google's super satellite captures first image," in *Wired*, <https://www.wired.com/2008/10/geoeye-1-super/> (2008).
40. M. Marcus and H. Minc, *A Survey of Matrix Theory and Matrix Inequalities*, Dover Publication, New York, (1992).
41. G. H. Golub and C. F. Van Loan, *Matrix Computations*, John Hopkins University Press, Baltimore (1983).
42. M. Moeller, T. Wittman, and A. L. Bertozzi, "A variational approach to hyperspectral image fusion," *Proc. SPIE* **7334**, 73341E (2009).

43. Q. Yan et al., "Single image superresolution based on gradient profile sharpness," *IEEE Trans. Image Process.* **24**(10), 3187–3202 (2015).
44. R. Keys, "Cubic convolution interpolation for digital image processing," *IEEE Trans. Acoust. Speech Signal Process.* **29**(6), 1153–1160 (1981).

Jin Zhou received his PhD in computer science and engineering from Arizona State University in 2009. He was with Signal Processing, Inc., between 2009 and 2013. He is currently with Google. He has worked on many projects including video processing and speech processing, fault location in power networks, speech enhancement in noisy environments, compressed sensing, and hyperspectral image processing.

Chiman Kwan received his BS degree with honors in electronics from the Chinese University of Hong Kong in 1988, and his MS and PhD degrees in electrical engineering from the University of Texas at Arlington in 1989 and 1993, respectively. Currently, he is the chief technology officer of Signal Processing, Inc., leading research and development efforts in chemical agent detection, biometrics, speech processing, fault diagnostics and prognostics, and image and video processing.

Bence Budavari received his BS degree in audio engineering technology from Belmont University, Nashville, TN, USA. He joined Signal Processing, Inc., in April 2016. He is currently working on mission planning systems for unmanned air vehicles, image fusion, and landing place identification.